

Alterations in the characteristic size distributions of subcellular scatterers at the onset of apoptosis: effect of Bcl-x_L and Bax/Bak

Jing-Yi Zheng

Nada N. Boustany

Rutgers University
Department of Biomedical Engineering
Piscataway, New Jersey 08854

Abstract. Optical scatter imaging is used to estimate organelle size distributions in immortalized baby mouse kidney cells treated with 0.4 μM staurosporine to induce apoptosis. The study comprises apoptosis competent iBMK cells (W2) expressing the proapoptotic proteins Bax/Bak, apoptosis resistant Bax/Bak null cells (D3), and W2 and D3 cells expressing yellow fluorescent protein (YFP) or YFP fused to the antiapoptotic protein Bcl-x_L (YFP-Bcl-x_L). YFP expression is diffuse within the transfected cells, while YFP-Bcl-x_L is localized to the mitochondria. Our results show a significant increase in the mean subcellular particle size from approximately 1.1 to 1.4 μm in both Bax/Bak expressing and Bax/Bak null cells after 60 min of STS treatment compared to DMSO-treated control cells. This dynamic is blocked by overexpression of YFP-Bcl-x_L in Bax/Bak expressing cells, but is less significantly inhibited by YFP-Bcl-x_L in Bax/Bak null cells. Our data suggest that the increase in subcellular particle size at the onset of apoptosis is modulated by Bcl-x_L in the presence of Bax/Bak, but it occurs upstream of the final commitment to programmed cell death. Mitochondrial localization of YFP-Bcl-x_L and the finding that micron-sized particles give rise to the scattering signal further suggest that alterations in mitochondrial morphology may underlie the observed changes in light scattering. © 2010 Society of Photo-Optical Instrumentation Engineers. [DOI: 10.1117/1.3462933]

Keywords: Bcl-2-family; mitochondria; light microscopy; light scattering; apoptosis.

Paper 10079R received Feb. 14, 2010; revised manuscript received Apr. 12, 2010; accepted for publication May 12, 2010; published online Jul. 16, 2010.

1 Introduction

There has been recent interest in studying the light scattering properties of cells undergoing apoptosis.¹⁻⁶ Light scattering methods, which do not require sample labeling, can be used to facilitate and improve the throughput of cell-based diagnostics and drug discovery. In the context of programmed cell death (apoptosis), light-scattering-based assays could be used to monitor rapidly and at low cost the effect of chemotherapeutic drugs *in vitro* and evaluate their effect on cells isolated from patient biopsies, thus creating the potential of investigating chemotherapeutic agents in a patient-based cell model. The premise behind such light scattering cell assays is that the measured optical scatter signals be specifically associated with the apoptosis process. As such, these dynamic signatures must be established and their specificity to programmed cell death determined. One way to address this is by demonstrating that the light scatter changes, which occur during apoptosis, can be modulated by molecular manipulations that up-regulate or inhibit apoptosis-specific molecular pathways.

Since Bcl-2 family proteins have been conclusively established as mediators of apoptosis,⁷ we have been interested in investigating whether light scattering by apoptotic cells can be modulated by pro- and antiapoptotic Bcl-2 family proteins. Bcl-2 family proteins, including Bcl-x_L, Bax, and Bak, share Bcl-2 homology (BH) domains and control apoptosis by interacting with each other via these domains.⁷⁻⁹ Bcl-2 proteins include multidomain proapoptotic proteins (e.g., Bax and Bak), multidomain antiapoptotic proteins (e.g., Bcl-2 and Bcl-x_L, MCL-1), and proapoptotic “BH3-only” proapoptotic proteins (e.g., Bid, Bad, Bim, Noxa, and Puma). Interaction between Bcl-2 family proteins involves the hydrophobic pocket formed by the close arrangement of the BH1-BH3 domains of a multidomain protein, and the exposed BH3 helix of another multidomain or BH3-only protein. Multidomain proteins also possess a hydrophobic C-terminal region, which can localize within organellar membranes, including the outer membrane of mitochondria. During apoptosis, Bax and Bak are activated and cause the release of proapoptotic factors such as cytochrome c from the mitochondrial intermembrane space.¹⁰⁻¹² This in turn activates caspases (proteases), resulting in nuclear fragmentation and cell death. Bax and Bak can

Address all correspondence to: N. N. Boustany, Ph.D., Dept. of Biomedical Engineering, Rutgers University, 599 Taylor Road, Room 320, Piscataway, NJ 08854. Tel: 732-445-4500 x6320; Fax: 732-445-3735; E-mail: nboustan@rci.rutgers.edu

be activated directly by interacting with proapoptotic BH-3-only proteins.¹³ On the other hand, the proapoptotic activity of Bax and Bak can be inhibited by interaction of Bax and Bak with antiapoptotic Bcl-2 family members such as Bcl-x_L.¹⁴⁻¹⁷ BH-3-only proteins can also activate Bax and Bak indirectly by binding and neutralizing antiapoptotic Bcl-2 family members.¹⁸

In a previous publication,² we reported that the scattering parameter optical scatter image ratio (OSIR), which gives a measure of subcellular particle size by measuring the ratio of wide-to-narrow angle scatter, decreases within the first 60 min of staurosporine (STS) treatment in CSM 14.1 cells. Overexpression of the antiapoptotic protein Bcl-x_L significantly slowed down this OSIR dynamic. We also reported that overexpression of Bcl-x_L could mediate changes in mitochondrial morphology in untreated cells. This resulted in a decrease in OSIR that was coincident with an increase in the proportion of mitochondria, with an expanded matrix having greatly reduced intracrystal spaces observed by electron microscopy.¹⁹ The change in mitochondria morphology and optical scatter was correlated with mitochondrial localization of Bcl-x_L, but not with cell death resistance, as expression of Bcl-x_L lacking the C-terminal transmembrane domain caused a significant level of cell death resistance but no measurable change in mitochondria or light scattering.¹⁹ Similarly, the previously observed effect of Bcl-x_L on slowing down the OSIR response to the STS challenge could be correlated with the antiapoptotic function of Bcl-x_L without excluding the possibility of observing optical scatter changes in apoptosis resistant cells, in which cell death resistance is imparted by a mechanism other than Bcl-x_L overexpression.

In this work, we further investigate the relationship between the measured optical scatter changes and cell death in response to staurosporine (STS) treatment. We use apoptosis-competent Bax/Bak expressing (W2) immortalized baby mouse kidney (iBMK) cells and apoptosis-resistant Bax/Bak null (D3) iBMK cells, in which apoptosis resistance is imparted by the absence of Bax/Bak.²⁰ We characterize the scattering changes using our previously developed optical scatter imaging method, and in this work use the method to provide estimates of particle size distributions with a model based on the Mie theory. Our results show that changes in light scattering within the first hour of STS treatment are not blocked by knockout of Bax/Bak. We also find that the effect of Bcl-x_L on slowing down the scattering response can be reproduced in the Bax/Bak expressing cells, but to a lesser extent in the Bax/Bak null cells, implying that the effect of Bcl-x_L on light scattering is diminished in the absence of Bax/Bak. Thus, it appears that the initial changes in subcellular structure are Bcl-x_L-specific. However, these changes appear to occur upstream of Bax/Bak activation and the final commitment to cell death.

2 Methods

2.1 Homogeneous Aqueous Suspensions of Spheres

Monodisperse polystyrene spheres (Polysciences, Warrington, Pennsylvania) with diameters of 0.356, 0.548, 0.771, and 1.053 μm were suspended in water and adjusted to have scattering coefficient $\mu_s \sim 0.01 \mu\text{m}^{-1}$. The refractive index of

polystyrene spheres is 1.6 and results in the index ratio $m = 1.2$ ($=n_{\text{polystyrene}}/n_{\text{water}}=1.6/1.33$). The aqueous sphere suspensions were sandwiched between a microscope slide and a 22 \times 22-mm coverslip separated by 75- μm -thick double-sided tape (Scotch[®], 3M), and then sealed with a 1:1:1v/v/v mixture of vaseline, lanolin, and paraffin (VALAP).

2.2 Molecular Biology and Generation of Stable Cell Lines

Immortalized baby mouse kidney (iBMK) cells, W2 cells, and iBMK cells lacking Bax and Bak (D3 cells) were generously provided by the laboratory of Dr. E. White at Rutgers University. iBMK cells were maintained at 38 °C in a 5% CO₂ in-air atmosphere in high glucose Dulbecco's Modified Eagles Medium (DMEM) supplemented with 10% fetal bovine serum (FBS) (V:V), 100-units/ml penicillin, and 100- μg /ml streptomycin. For microscopy, cells were cultured on glass cover slips, to which they readily attach. The preparation of iBMK cells that stably expressed YFP and YFP-Bcl-x_L was described previously.¹⁹ Expression of YFP constructs was confirmed by fluorescence microscopy of the live cells. YFP fluorescence was detected with a YFP filter cube (Carl Zeiss Filter 46), excitation bandpass: 500 \pm 10 nm, emission filters: >515 nm long-pass dichroic filter, followed by a 535 \pm 15 nm bandpass filter. Since the overexpressed Bcl-x_L was linked to YFP, we used the YFP-transfected cells to control the effects of YFP transfection.

2.3 Optical Scatter Image Acquisition and Analysis

The optical scatter imaging setup used here was described previously.¹⁹ The wavelength of the incident light on the sample was 630 nm \pm 5 nm. The images were collected using an oil immersion objective, NA=1.4. In a Fourier plane conjugate with the objective's back focal plane, a variable iris diameter with a center beam stop was switched between high numerical aperture (NA) and low NA positions, collecting light within a solid angle bound at the oil immersion objective by 3 deg < θ_{HNA} < 90 deg for high NA, and 3 deg < θ_{LNA} < 10 deg for low NA. The angles 3, 10, and 90 deg are set by the radius of the beam block in the center of the variable diameter iris, the edge of the iris used for the low NA acquisition, and the numerical aperture of the objective, respectively. These angles were measured using the diffraction pattern of a graticule with spacing $b = 10 \mu\text{m}$ in the object plane. These scattering angle ranges, which were reported previously,¹⁹ are corrected here to account for the index mismatch between the aqueous culture medium ($n = 1.33$) and the 63 \times objective's immersion oil ($n = 1.5$). When corrected for the index mismatch between water and oil, these angular ranges result in collecting light scattered by the sample within a solid angle bound by 3.38 deg < θ_{HNA} < 90 deg for high NA, and 3.38 deg < θ_{LNA} < 11.29 deg for low NA. As before, the ratio of high-to-low NA background-subtracted signal was measured at each pixel in the image and defined as the OSIR. The OSIR was subsequently converted to particle diameter, as described in the next section.

Each coverslip with attached live cells was mounted by means of a steel plate onto the stage of the inverted microscope. Just before mounting onto the microscope's stage, the DMEM growth medium was replaced with Leibovitz L15 me-

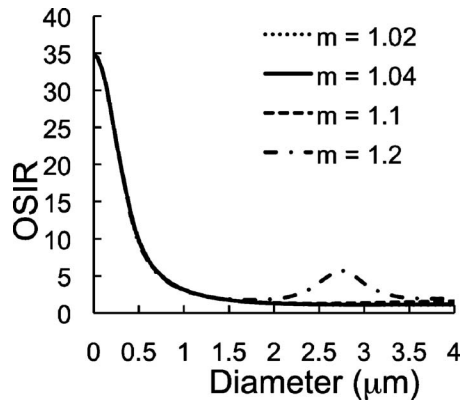


Fig. 1 Numerical simulations of light scattering by spheres with index ratio $m=1.02$ (dot), $m=1.04$ (line), $m=1.1$ (dash), and $m=1.2$ (dash dot). The simulations were done with an x -parameter increment of 0.1 for the range $x=0.1$ to 1, and an x parameter increment of 1 for $x > 1$. $x = \pi D n / \lambda$, $\lambda = 0.630 \mu\text{m}$, $n = 1.33$.

dium (Invitrogen, Carlsbad, California) supplemented with 10% fetal bovine serum, 100-units/ml penicillin, and 100-mg/ml streptomycin. Leibovitz's L15 was used to maintain the cells in a non- CO_2 -equilibrated environment and did not contain phenol red, whose color could cause light absorption. The cells were monitored by DIC, fluorescence, and optical scatter microscopy at room temperature and room air.

Optical scatter images were acquired in IPlab (BD Biosciences Bio-imaging, Rockville, Maryland) and processed in MatLab (The MathWorks, Natick, Massachusetts). In each experiment, a segment was manually defined around every cell in the differential interference contrast (DIC) images. These segments were overlaid onto the optical scatter images such that data analysis was limited to regions containing a cell. Only positively fluorescent cells were analyzed in the transfected cell variants. An OSIR threshold, 1.15 to 40, was applied and only pixels within this range were analyzed. The upper and lower thresholds were used to exclude values of OSIR that fell outside of the theoretical expected range. An upper value of 40 was conservatively chosen to account for noisy data. These threshold values exclude $\sim 20\%$ of the pixels within a typical cell.

2.4 Conversion of Optical Scatter Image Ratio Pixel Histograms to Particle Size Distributions

The optical scatter images directly encode at each pixel the measured value of the OSIR, corresponding to the intensity ratio of high-to-low NA scatter. For spheres, this intensity ratio was inferred from the Mie theory²¹ as:

$$\text{OSIR} = \frac{\int_{\phi=0}^{360 \text{ deg}} \int_{\theta=3.38 \text{ deg}}^{\theta=90 \text{ deg}} T(\theta) F(\theta, \phi) \sin \theta d\theta d\phi}{\int_{\phi=0}^{360 \text{ deg}} \int_{\theta=3.38 \text{ deg}}^{\theta=11.29 \text{ deg}} T(\theta) F(\theta, \phi) \sin \theta d\theta d\phi}, \quad (1)$$

where $F(\theta, \phi)$ is the scattering phase function, θ is the scattering angle with respect to the incident direction, and ϕ is the azimuthal angle of scatter. The scattering phase function was weighted by the Fresnel transmittance coefficients $T(\theta)$ at each scattering angle incident on the water-glass/oil interface. Equation (1) was utilized to generate simulated OSIR values for spheres of different diameters (Fig. 1). Based on this

model, the pixel histograms of the optical scatter images can therefore be converted to particle diameter distributions to provide a morphometric length scale. For this, pixel histograms of the optical scatter images were generated by binning the OSIR values into elements with 0.1 intervals. The OSIR value of each bin was converted to diameter value by interpolating the simulated sphere data (Fig. 1). This conversion results in a histogram depicting the number of pixels at each diameter.

We used the $m=1.04$ data in Fig. 1 to convert the cell OSIR to diameter, and the $m=1.2$ curve to convert the sphere suspension OSIR data. Moreover, in the case of the polystyrene spheres with $m=1.2$, the largest diameter tested was $1.053 \mu\text{m}$ to remain in the monotonically decreasing region of the curve. With refractive index ratio $m=1.04$, the calculated OSIR based on the Mie theory decreases nonlinearly and monotonically from 34.65 to 1.15 as a function of sphere diameter for diameter values going from 0.01 to $2.38 \mu\text{m}$. Beyond diameters of $2.38 \mu\text{m}$, the OSIR value does not decrease monotonically but remains under 1.15. Below diameters of $0.01 \mu\text{m}$, the calculated OSIR changes negligibly but remains above 34.65. Thus, cell pixels with OSIR less than 1.15 or OSIR greater than 34.65 were not considered in this histogram analysis. In the OSIR range 1.15 to 40, less than 0.05% of the total pixels exist between 34.65 and 40.

The histograms of pixel distribution as a function of diameter were further analyzed by converting the number of pixels at each diameter to number of particles N to yield a particle size distribution. At each diameter D the number of particles N was calculated as $N = (\text{number of pixels} \times a) / \pi(D^2/4)$, where a is the area of one image pixel in the object plane, and making the simple assumption that the particles are on average sectioned across their midline in the plane of the image. The pixel area a corresponded to a $0.49 \mu\text{m} \times 0.49 \mu\text{m}$ area in the object based on the image of a calibrated graticule. For the cell data, the number of particles at each diameter was normalized to the number of cells tested to yield a 2-D particle size distribution per cell. For all sphere samples, the tested sample area was $250 \times 250 \mu\text{m}$.

2.5 Apoptosis Experiments

With the cells on the microscope stage, apoptosis was induced by replacing the L15 growth medium with the same supplemented with $0.4 \mu\text{M}$ staurosporine (STS) (Sigma Chemical, Saint Louis, Missouri) prepared from a 4 mM stock solution of STS in DMSO. Treatment with the same volume of DMSO in L15 growth medium, but without STS, was used as a negative control.

2.6 Cell Death Assay

Cell death resistance was assessed by measuring the percentage of dead cells in response to STS treatment. Cells were cultured in 12-well plates, and treated with $0.4 \mu\text{M}$ STS at 90% confluence. After 24 h, 40-mM propidium iodide (Invitrogen) was added to the incubated cultures for 15 min. The cells were collected from the plates by pipetting and trituration. Microscopic observation of the plates insured that all cells were collected by this process. The cell suspension was concentrated to $\sim 5 \times 10^5$ cells/ml by centrifugation and partial removal of the supernatant. The number of cells with posi-

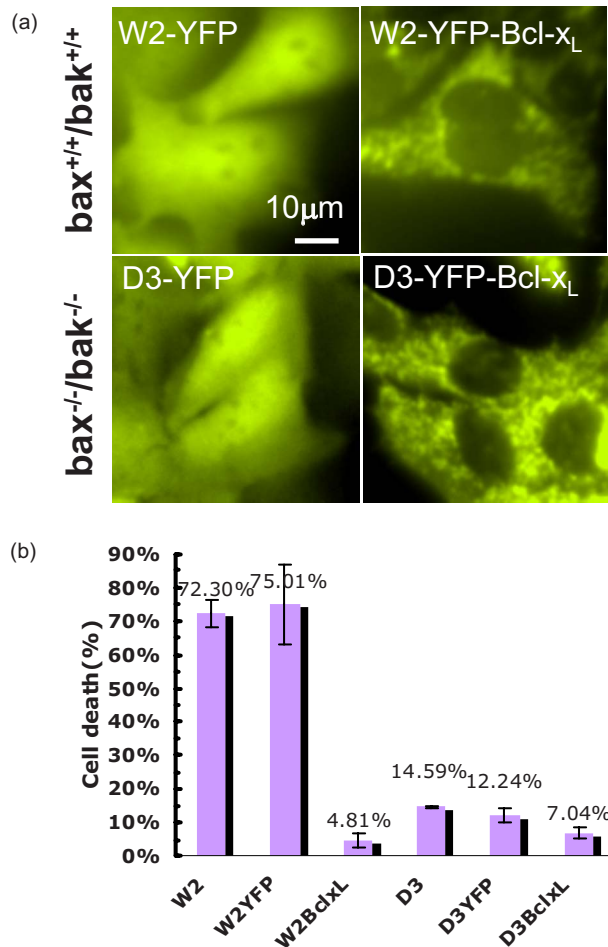


Fig. 2 (a) Fluorescence images of the transfected iBMK cell variants. W2 express Bax/Bak and D3 are Bax/Bak null. The transfectants stably expressed YFP or YFP-Bcl-x_L. (b) Percentage of dead iBMK cells assessed by propidium iodide exclusion after 24 h of treatment with 0.4-μM STS. Error bars represent the standard deviation of the mean of at least three different culture plates.

tive propidium iodide fluorescence in the final cell suspension was counted in a hemacytometer, and was taken as the number of dead cells that had lost membrane integrity. Propidium iodide fluorescence was visualized with a rhodamine filter cube (filter number 20, Carl Zeiss). The results from at least three different culture plates were analyzed under each condition.

3 Results

3.1 Effect of Bcl-x_L and Bax/Bak on Staurosporine-Induced Cell Death

Figure 2(a) shows images of the transfected Bax/Bak expressing (W2) and Bax/Bak null (D3) iBMK cells. YFP expression resulted in diffuse fluorescence throughout the cells, while expression of YFP-Bcl-x_L showed a filamentous pattern consistent with mitochondrial localization. To confirm the anti-apoptotic effect of Bcl-x_L, we challenged the cells with STS to induce apoptosis and measured the percentage of dead cells. After 24 h of treatment with 0.4 μM STS, the percentage of dead cells was 72.30 ± 4.09% and 75.01 ± 11.76% for

W2 cells and W2 cells expressing YFP, respectively [Fig 2(b)]. W2 cells overexpressing YFP-Bcl-x_L were resistant to cell death with only 4.81 ± 2.18% dead cells. iBMK D3 cells, which lack the proapoptotic proteins Bax and Bak, and YFP expressing D3 cells showed only 14.59 ± 0.46% and 12.24 ± 2.21% cell death, respectively. Overexpression of YFP-Bcl-x_L in the D3 cells further decreased cell death to 7.04 ± 1.53%. The inhibition of cell death by Bcl-x_L overexpression and by knockout of Bax/Bak also supports the fact that apoptosis is the cell death process being induced by STS.

3.2 Alterations in Light Scattering at Onset of Apoptosis

In a previous publication,² STS treatment caused a decrease in OSIR by ~25% from baseline in nontransfected CSM 14.1 and YFP expressing CSM14.1 cells. In contrast, the OSIR decreased by less than 10% after STS treatment in the CSM cells expressing YFP-Bcl-x_L. To investigate the reproducibility of these results, we performed the same experiment on the Bax/Bak expressing iBMK W2 cells and their transfected variants (Figs. 3 and 4). The OSIR per cell was first calculated by averaging the OSIR pixel values within each cell segment. In Fig. 3, the average OSIR per cell was also normalized to the initial OSIR value immediately after STS addition ($t=0$). The OSIR averages reported in Fig. 3 (red lines) and Fig. 4 are subsequently calculated by averaging the OSIR values per cell over the cell population under a given condition. The nontransfected W2 cells and YFP-W2 variants showed an average ~32% and ~20% OSIR decrease, respectively, and the YFP-Bcl-x_L W2 variant showed only ~8% decrease in the average OSIR per cell after treatment with STS for 60 min. Changes in OSIR were 3% after 60 min of DMSO treatment in the absence of STS. To further investigate the relationship between the initial OSIR decrease and apoptotic cell death, we measured the OSIR response to STS challenge in the apoptosis-resistant Bax/Bak null iBMK D3 cells. Nontransfected D3, YFP-D3, and YFP-Bcl-x_L-D3 variants all showed a monotonic decrease in OSIR. The decrease in OSIR after 60 min of STS treatment was 26% for D3, 29% for YFP-D3, and 16% for YFP-Bcl-x_L D3 cells. The slight increase in OSIR after 40 min for D3 and D3-YFP-Bcl-x_L was not statistically significant. Individual OSIR cell traces (gray lines) are displayed in Fig. 3, along with the average (red lines in Fig. 3) for each cell variant treated with STS. Although the average responses of the nontransfected W2 and D3 cells are similar, the W2 cell responses are more heterogeneous. In both variants, the OSIR responses of some cells also increased first and then decreased. The nonnormalized initial OSIR values at $t=0$ just prior to STS treatment and final values after 60 min of STS treatment are shown in Fig. 4 for all the cell variants. The decrease in OSIR in the W2 cells and its inhibition by overexpression of Bcl-x_L reproduce the trends observed previously in the CSM14.1 cells.² However, unlike the previously tested CSM 14.1 cells, the YFP-Bcl-x_L expressing W2 cells had a similar initial OSIR compared with their parental W2 counterparts.

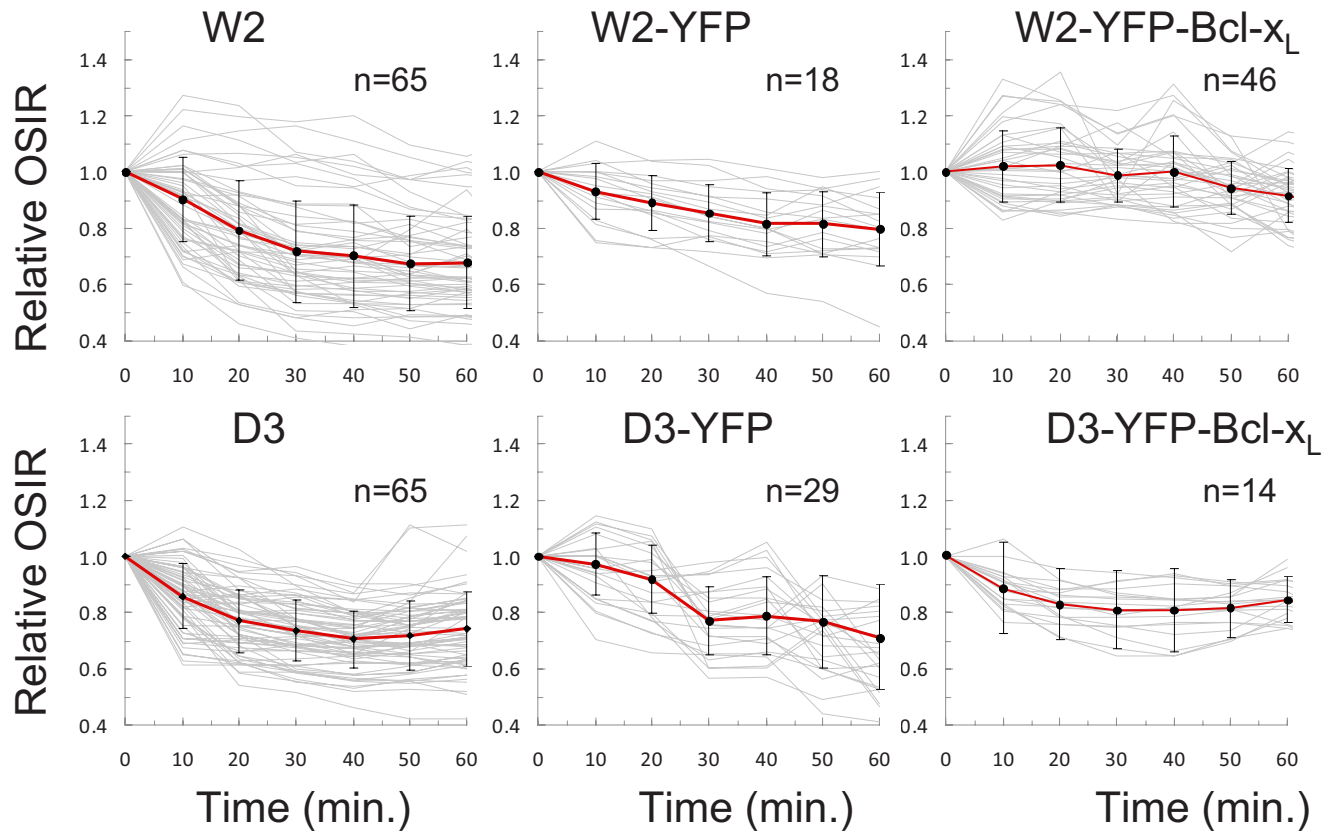


Fig. 3 Relative OSIR changes in individual cells (gray lines) treated with STS. The red lines are the average responses of all the cells tested (the number of cells tested in each case is reported on each panel). For each cell (each individual gray trace), the OSIR value at a given time point corresponds to the average OSI pixel value within that cell's segment normalized to the initial average OSI pixel value at time=0 min. just before STS treatment. The red traces show the mean \pm the standard error of the mean of these normalized average OSIR values calculated on a cell-by-cell basis. (Color online only.)

3.3 Alterations in Light Scattering versus Cell Morphology

STS is a general kinase inhibitor^{22,23} and causes cell shrinkage. We first investigated cell shrinkage by observing cellular morphology with differential interference contrast (DIC) and

compared these images with the optical scatter images of the different cell variants before and after 60 min of STS treatment (Fig. 5). All variants, except the W2 and D3 cells expressing YFP-Bcl-x_L, appeared shrunken after STS challenge. The fact that the D3 YFP-Bcl-x_L cells did not shrink but still showed an OSIR decrease in response to STS suggests that the OSIR decrease is not due to the shrinkage of the cells but is more likely due to the morphological alteration of subcel-

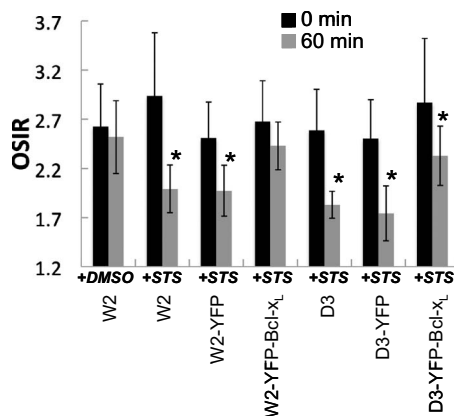


Fig. 4 Average OSIR values per cell before treatment (black bars, 0 min) and 60 min after treatment with either DMSO or STS (gray bars). Data are the mean OSIR per cell \pm the standard deviation of the mean. The star indicates a p value < 0.001 based on a Student t -test (comparing values at 0 min with those at 60 min in each case).

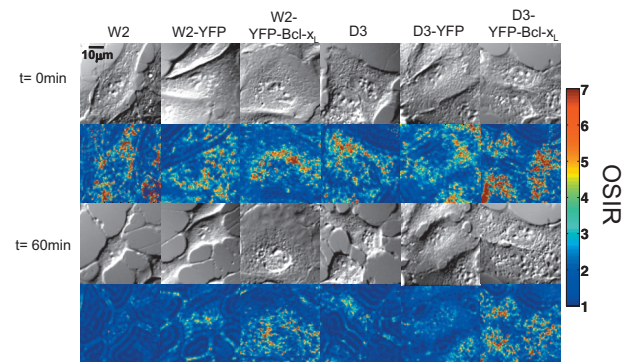


Fig. 5 DIC and OSI images of nontransfected, YFP-expressing, and YFP-Bcl-x_L-expressing W2 and D3 cells before ($t=0$ min) and after ($t=60$ min) treatment with $0.4 \mu\text{M}$ STS.

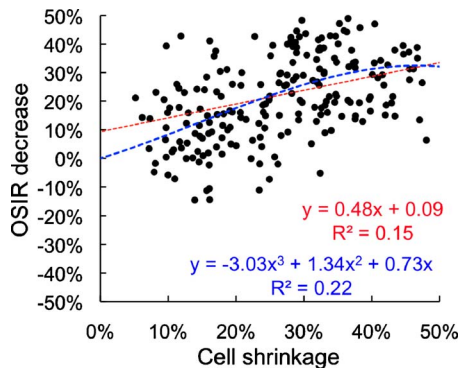


Fig. 6 OSIR decrease versus cell shrinkage after 60 min of STS treatment. The red dashed line is a linear fit to the data, and the blue dashed line is a third order polynomial fit. Each black dot represents a single cell (data include all W2, D3, and variants). (Color online only.)

ular organelles. To further confirm that the OSIR decrease is not correlated with cell shrinkage, we plotted the percentage OSIR decrease versus percentage cell shrinkage between 0 and 60 min for all the cells tested (Fig. 6). The decrease in cell area was estimated by counting the number of pixels with “active” OSIR values between 1.15 and 40 within each cell. While this excludes some background regions within the cells, this number of pixels was linearly correlated (correlation value >0.9) with the area of the cell measured by segmentation of the DIC images. Thus, we used the percent decrease in the number of active OSIR pixels as a measure for cell shrinkage. The plot in Fig. 6 shows little correlation between the decrease in OSIR and cell shrinkage with low correlation values (R^2), whether a linear or polynomial fit to the data is used ($R^2=0.15$ and $R^2=0.22$, respectively). Moreover,

STS-induced cell shrinkage is not related to sensitivity or resistance to apoptosis, since both the W2 and D3 cells shrunk in the first 60 min of STS treatment.

After 24 h of treatment, all cells, including the propidium iodide negative or apoptosis resistant cells, were rounded up (data not shown) and could be collected easily by pipetting up and down. Thus, Bcl-x_L only delayed the cell shrinkage induced by STS, and this effect does not depend on Bax/Bak, as the cell shrinkage was delayed in both W2 and D3 cell variants.

3.4 Estimated Particle Size Distribution of Spheres in Aqueous Suspensions

The OSIR pixel histograms were converted to particle size distributions as described in Sec. 2.4 to get an estimate of subcellular particle size. We first applied the method to aqueous polystyrene spheres as model particles of known size. Figure 7(b) shows the pixel histograms obtained from the optical scatter images of the spheres [Fig. 7(a)]. Figure 7(c) shows the corresponding particle diameter distributions obtained from the conversion of the pixel histograms. The mean diameter \pm standard deviation of 0.356, 0.548, 0.771, and 1.053- μm spheres are 0.332 ± 0.044 , 0.521 ± 0.072 , 0.638 ± 0.151 , and 0.800 ± 0.212 μm , respectively. The peak histogram values were 0.357, 0.529, 0.669, and 0.83 μm . Fitting the distributions to a Gaussian, we retrieved means and standard deviations of 0.361 ± 0.096 , 0.538 ± 0.121 , 0.701 ± 0.211 , and 0.929 ± 0.309 μm ($\mu \pm \sigma$), respectively. These values were more representative of the actual sphere diameters, especially for larger diameters where the measured particle distribution is skewed to the right due to the inability to interpret the lower OSIR values outside the dynamic range. The histograms show good discrimination between the different particle sizes. However, the variance in the estimated di-

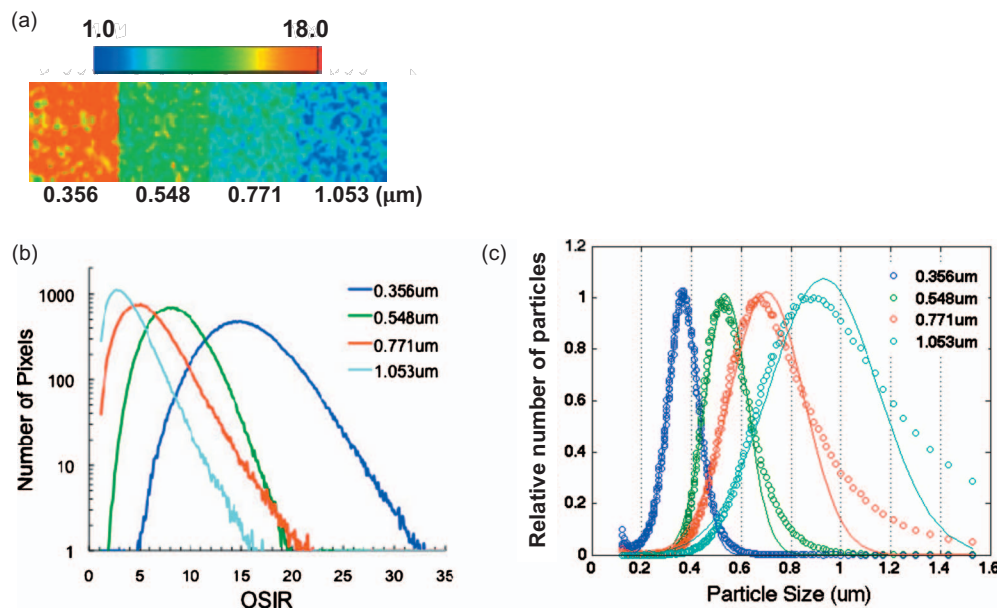


Fig. 7 (a) OSI images of aqueous polystyrene sphere suspensions with diameters 0.356, 0.548, 0.771, and 1.053 μm . (b) OSI pixel histograms corresponding to the images shown in (a). (c) Particle diameter distributions obtained from the OSI pixel histograms. The distributions are shown normalized to the maximum number of particles.

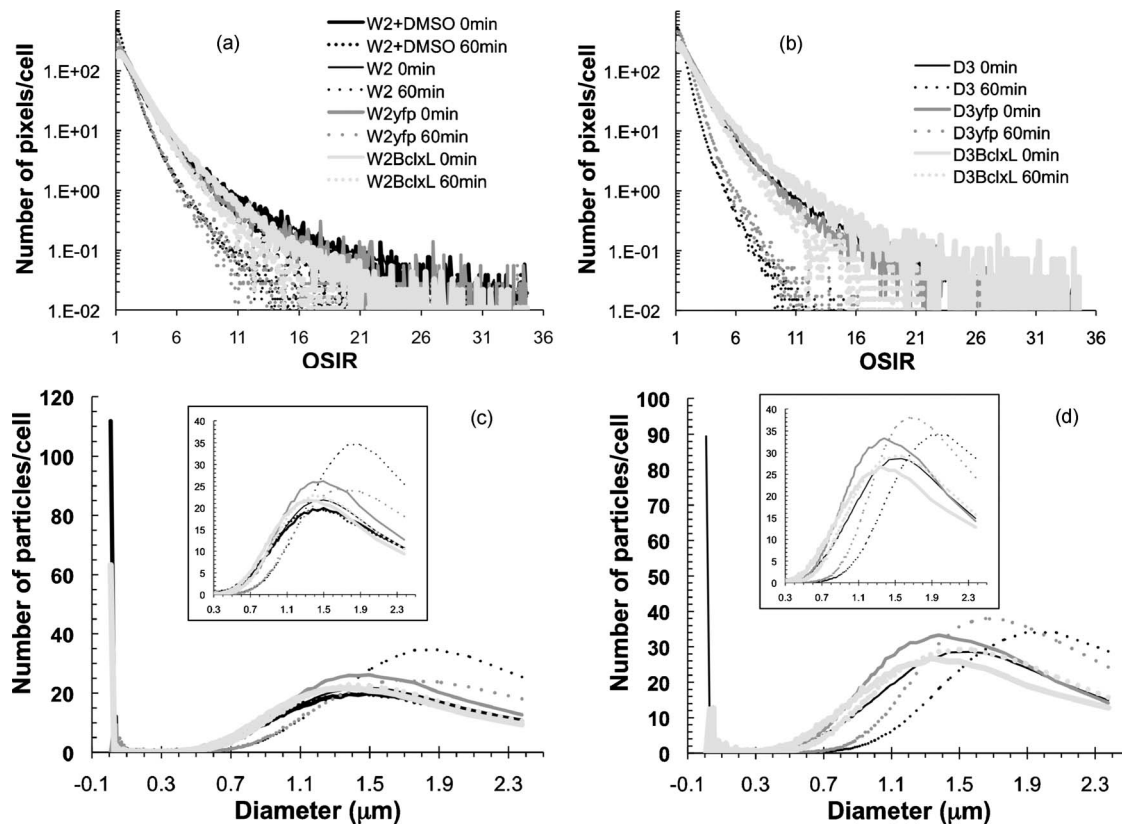


Fig. 8 OSI pixel histograms of (a) W2 and (b) D3 cell variants shown before (solid lines) and after (dotted lines) 60 min of treatment with STS or DMSO. Particle size distribution of W2 (c) and D3 (d) cell variants before (solid lines) and after (dotted lines) 60 min of treatment with STS or DMSO. The distributions were obtained by converting the corresponding histograms in (a) and (b). In (c) and (d) we included an inset to magnify the histograms for diameters above $0.3 \mu\text{m}$.

ameter increases from ~ 18 to 30% as particle diameter increases and is significantly larger than the expected variance of 2 to 3% given by the sphere manufacturer. The measured variance in OSIR pixel value across the image of a given sphere suspension [Fig. 7(a)] is the initial source of these errors. While the mean OSIR value measured is representative of the sphere size, image pixel values can vary significantly due to movement of the spheres and diffraction in cases where the pixel size is smaller than the particle's geometric cross section. The increase in variance for larger particles is likely due to the "flattening" of the OSIR decrease at high diameters (Fig. 1). Thus, small changes in OSIR at diameters greater than $0.8 \mu\text{m}$ correspond to large relative changes in size, whereas large OSIR changes for diameters less than $0.5 \mu\text{m}$ correspond to small changes in size.

3.5 Estimated Subcellular Particle Size Distributions

Figures 8(a) and 8(b) show the pixel histograms of the W2 and D3 variants, respectively. The solid lines are the histograms before STS treatment ($t=0$ min) and the dotted lines are the histograms after 60 min of treatment with STS. The OSIR pixel histograms are shown after normalization to the number of cells. The histograms were converted to particle size distributions [Figs. 8(c) and 8(d)]. Figures 9(a) and 9(b) show the means and standard deviations of the particle size distributions as a function of time after treatment. The subcellular particle size distributions are broad with standard deviations

on the order of 40%. Consistent with the average OSIR decrease measured on the cell-by-cell basis (Figs. 3 and 4), the mean of the histogram, which gives an estimate of mean subcellular particle diameter, increases for the W2 (0.95 to $1.40 \mu\text{m}$) and D3 (1.08 to $1.53 \mu\text{m}$) cells and their YFP transfected counterparts (1.12 to $1.32 \mu\text{m}$ for W2-YFP and 1.08 to $1.42 \mu\text{m}$ for D3_YFP) after treatment with STS for 60 min. The mean diameter remains largely unchanged for the DMSO treated cells (1.04 to $1.08 \mu\text{m}$) and the W2 cells transfected with YFP-Bcl- x_L (1.05 to $1.14 \mu\text{m}$). In contrast, the histogram mean increased for the YFP-Bcl- x_L -D3 cells (0.99 to $1.15 \mu\text{m}$), but this increase was less pronounced than that observed in the untransfected D3 or YFP-D3 cells. Analysis of the histograms also retrieved a population of particles with sizes smaller than 100 nm, corresponding to pixels with OSIR values above ~ 34.65 . Due to the sparse number of particles in this size range, it was difficult to discern differences between the cell variants. However, the data suggest that there may be an overall lower number of particles in this nanoscale size range in the Bax/Bak null D3 cells compared with the W2 cells.

4 Discussion

We measured the ratio of wide-to-narrow angle scatter, OSIR, as a function of time in response to STS-induced apoptosis in iBMK cells expressing Bax/Bak (W2) and isogenic apoptosis

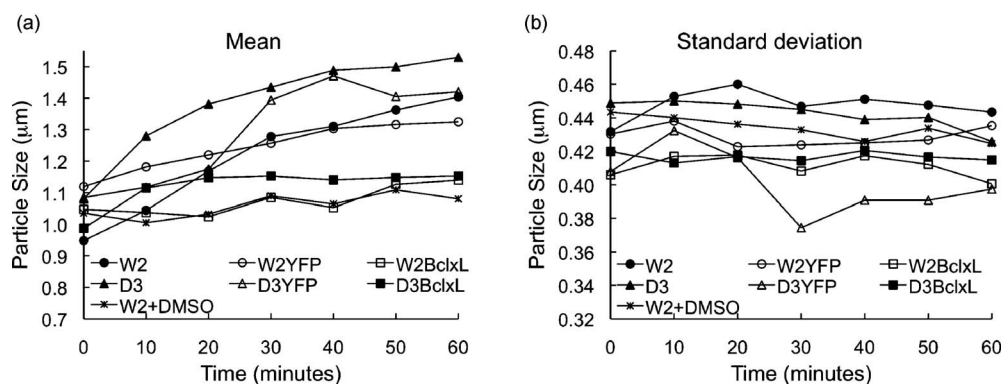


Fig. 9 (a) Means and (b) standard deviations of the subcellular particle size distributions as a function of time.

resistant iBMK cells lacking Bax/Bak (D3). The cells were also transfected with YFP-Bcl-x_L and YFP to study the effect of Bcl-x_L on light scattering in the W2 and D3 cell lines. The nontransfected cells and cells transfected with YFP showed a significant decrease in the OSIR value after treatment with STS compared with control W2 cells treated with only DMSO. The changes in OSIR were absent in the W2 cells expressing YFP-Bcl-x_L, but were not completely blocked in the D3 cells expressing YFP-Bcl-x_L (Figs. 3, 4, and 8). Since all D3 cell variants are resistant to apoptosis (Fig. 2) and still exhibited the OSIR decrease, the measured OSIR decrease is not correlated with the final commitment to cell death mediated by Bax/Bak. However, the scattering dynamics could be inhibited by Bcl-x_L, suggesting that Bcl-x_L modulates subcellular morphology upstream of Bax/Bak. Furthermore, the effect of YFP-Bcl-x_L on blocking the OSIR decrease was more pronounced in the W2 cells compared with the D3 cells (D3 YFP-Bcl-x_L). This suggests that the effect of Bcl-x_L on light scattering is dependent on the presence of Bax/Bak. Whether the effect of Bcl-x_L on modulating subcellular morphology at the initiation of apoptosis is related to its ability to confer cell death resistance remains to be confirmed.

The measured decrease in OSIR was not correlated with cell shrinkage. This is consistent with the fact that the measured OSIR corresponds to particle sizes in the range $0.01 \mu\text{m} < D < 2.38 \mu\text{m}$. Since the cell diameter is larger than $10 \mu\text{m}$, even after shrinking, the change in cell size should not be reflected in the OSIR measurement. The lack of correlation between OSIR decrease and cell shrinkage also suggests that the OSIR decrease is not related to the rearrangement of subcellular particles due to cell rounding.

The initial average OSIR values did not differ significantly for the iBMK cell variants studied here. Thus, unlike our previously tested nigral CSM14.1 cells, iBMK cells expressing YFP-Bcl-x_L did not have a markedly lower OSIR compared to their parental or YFP transfected counterparts (Fig. 4). As such, the effect of Bcl-x_L on the baseline light scattering properties of untreated cells may be cell-type dependent. W2 iBMK cells also exhibited more cell-to-cell variability than the other variants used in this study. Clonal transfected cells may show less variability due to the selection of specific clones. What may be surprising is higher variability in the W2 cells compared with the D3 cells, which are obtained from transgenic mice. Understanding how the preparation of vari-

ous cell lines can result in a more or less diverse cell population remains to be determined. As with most biological data, the statistical significance of our data ultimately reflects on the average behavior of a given cell population. While the diversity of biological cells within a given population may be difficult to explain, the presence of such heterogeneity supports the use of the OSI technique, which allows us to analyze the scattering properties of single cells.

Since OSIR is a function of sphere diameter, we were able to convert our pixel histograms to particle size distributions for samples consisting of sphere suspensions. This conversion was essentially based on the assumption that the scattering signal is uniform over the dark-field image of a given sphere. However, in reality, each sphere was not stationary and occupied more pixels than its actual size due to diffraction. These effects gave rise to variations in the estimated sphere sizes that were larger than expected. Still, the mean sphere diameters measured were close to the actual sphere diameters. This was especially the case of the smaller spheres (0.356 and $0.548 \mu\text{m}$), whose size was smaller than, or on the order of, the image pixel size and whose fast Brownian motion could be averaged over the image acquisition time. In addition, in the case of $m=1.2$, the OSIR remains monotonic only for diameters less than $<1.43 \mu\text{m}$, introducing an error in the conversion of pixels with OSIR value under ~ 5 (Fig. 1). Hence the particle size distribution of smaller particles had more symmetric Gaussian-shaped distributions.

The histogram conversion was applied to get particle size distributions for the cell variants tested. In this case, a refractive index ratio $m=1.04$ was used, and the OSIR decreases monotonically going from a diameter of 0.01 to $2.38 \mu\text{m}$. An index ratio of $m=1.04$ was taken as being generally representative of the index ratio between organelles and cytoplasm, which generally remains close to 1.²⁴ This assumption is supported by the negligible variation in the curves of Fig. 1 for values of m under 1.1. In the present setup, the scatter intensity was also averaged in the azimuthal scatter direction ϕ . Since organelles are not generally spherical, our histograms only provide an estimation of characteristic particle size distribution. Relative changes in this distribution are therefore more relevant than retrieving absolute size values. In this respect, we find that the distribution of particles on the order of $1 \mu\text{m}$ is affected by STS treatment (Figs. 8 and 9). Overex-

pression of YFP-Bcl-x_L, which localized to the mitochondria, could inhibit this change in particle size distribution. Thus the changes are likely to involve mitochondria whose size is on the order of 1 μm. Scatter anisotropy in the ϕ direction, which may give information about particle shape for non-spherical particles, could be measured by redesigning the iris to take the changes in intensity as a function of ϕ into account. An example of how this can be achieved is described in Ref. 25.

While the data in Fig. 7(c) suggest that there is a relatively large source of error when the OSIR pixel data are used to predict diameter, the particle size distributions in the cells are wider than the sphere size distributions, suggesting that the biological variability of particle sizes within a cell is larger than the particle size error associated with this method. The error in predicting diameter applies equally to all the cells tested in this work. Thus, conclusions based on comparison of relative changes in diameter remain valid. Interestingly, despite the inaccuracies involved in calculating our particle size distributions, the distributions found here are consistent with those reported and showing a significant contribution of micron-sized scatterers.^{26,27} We also noticed a population of particles $0.01 < D < 0.1$ μm, which roughly coincides with the reported population of scattering centers under 100 nm in both EMT6²⁷ and AT3.1 cells.²⁶ However, the relative size of this peak compared to the rest of the distribution is smaller in our data compared with previous reports.^{26,27} Due to our ratiometric measurement, our histograms are inherently normalized to the scattering cross sections at each diameter. However, the low-scattering cross section of particles in this nanoscale size range compared with larger particles may still limit our ability to isolate and detect their individual signal in imaged submicron locations within thin monolayers of cells. Since each image pixel corresponds to a $0.49 \mu\text{m} \times 0.49 \mu\text{m}$ area in the object, we also assume in our analysis that all the particles within a $0.49 \mu\text{m} \times 0.49 \mu\text{m}$ cellular cross section have the same diameter. The validity of this assumption is ultimately determined by how large the pixel bin is compared to the length scale over which the landscape of the cell remains purely homogeneous. If the pixel bin is larger than this length scale, we would underestimate the width of the particle size distribution. Going to an extreme, if the cells were sampled by one large pixel, our assumption would lead to a histogram with a single point corresponding to a single diameter value. If the pixel is then decreased from this maximum size to its minimum possible size, the single point histogram will get decomposed into individual peaks at the different diameters present in the cell. Ultimately, it will reach a maximum width constrained by diameters of the smallest and largest subcellular particles. While we do not have an independent measure of subcellular spatial heterogeneity in this study, the validity of our assumption regarding the inclusion of a single diameter value within each pixel is borne out by the fact that our histograms in Figs. 8(c) and 8(d) are qualitatively similar to published subcellular particle size distributions obtained via different methods of optical scatter measurements.^{26,27} Still, the size averaging over $0.49 \mu\text{m} \times 0.49 \mu\text{m}$ regions may have resulted in the underestimate of the number of particles under 100 nm.

In summary, the changes in OSIR measured at the onset of apoptosis induced by staurosporine are specific to the apoptosis pathway to the extent that they are modulated by Bcl-x_L, a protein conclusively shown to confer apoptosis resistance.⁷ However, the presence of these light scattering changes cannot be used to predict the final fate of the cells. The changes occur too early, such that other factors can intervene with cell death downstream (e.g., Bax/Bak knock-out). While the absence of light scattering changes may be correlated with cell death resistance mediated by Bcl-x_L, the presence of light scattering changes does not preclude cell death resistance via other means. In general, OSIR changes can be used to monitor relative changes in the characteristic size distributions of subcellular particles as a function of time. Thus, further monitoring of the OSIR beyond 60 min could ultimately reveal specific subcellular dynamics that more generally correlate with apoptotic cell death.

Acknowledgments

We thank Eileen White and members of the White Laboratory for generously providing the iBMK cells and associated culture protocols. We wish to thank August Miller (University of New Mexico) for his MieTab open source code, and Charles DiMarzio for insightful discussions about the effects of the water/oil interface. This work was supported in part by Biomedical Engineering Research grant number RG-02-0682 from the Whitaker Foundation, the Johnson and Johnson Discovery Awards Fund at Rutgers, The State University of New Jersey, and NSF grant DBI-0852857 to N. Boustany.

References

1. N. N. Boustany, S. C. Kuo, and N. V. Thakor, "Optical scatter imaging: subcellular morphometry *in situ* with Fourier filtering," *Opt. Lett.* **26**(14), 1063–1065 (2001).
2. N. N. Boustany, Y. C. Tsai, B. Pfister, W. M. Joiner, G. A. Oyler, and N. V. Thakor, "BCL-x(L)-dependent light scattering by apoptotic cells," *Biophys. J.* **87**(6), 4163–4171 (2004).
3. J. D. Wilson, B. R. Giesselman, S. Mitra, and T. H. Foster, "Lysosome-damage-induced scattering changes coincide with release of cytochrome c," *Opt. Lett.* **32**(17), 2517–2519 (2007).
4. I. Itzkan, L. Qiu, H. Fang, M. M. Zaman, E. Vitkin, I. C. Ghiran, S. Salahuddin, M. Modell, C. Andersson, L. M. Kimerer, P. B. Cipoloni, K. H. Lim, S. D. Freedman, I. Bigio, B. P. Sachs, E. B. Hanlon, and L. T. Perelman, "Confocal light absorption and scattering spectroscopic microscopy monitors organelles in live cells with no exogenous labels," *Proc. Natl. Acad. Sci. U.S.A.* **104**(44), 17255–17260 (2007).
5. C. S. Mulvey, A. L. Curtis, S. K. Singh, and I. J. Bigio, "Elastic scattering spectroscopy as a diagnostic tool for apoptosis in cell cultures," *IEEE J. Sel. Top. Quantum Electron.* **13**(6), 1663–1670 (2007).
6. K. J. Chalut, J. H. Ostrander, M. G. Giacomelli, and A. Wax, "Light scattering measurements of subcellular structure provide noninvasive early detection of chemotherapy-induced apoptosis," *Cancer Res.* **69**(3), 1199–1204 (2009).
7. S. Cory and J. M. Adams, "The BCL2 family: regulators of the cellular life-or-death switch," *Nat. Rev. Cancer* **2**(9), 647–656 (2002).
8. S. W. Muchmore, M. Sattler, H. Liang, R. P. Meadows, J. E. Harlan, H. S. Yoon, D. Nettekheim, B. S. Chang, C. B. Thompson, S. L. Wong, S. C. Ng, and S. W. Fesik, "X-ray and NMR structure of human Bcl-x_L, an inhibitor of programmed cell death," *Nature* **381**, 335–341 (1996).
9. M. Sattler, H. Liang, D. Nettekheim, R. P. Meadows, J. E. Harlan, M. Eberstadt, H. S. Yoon, S. B. Shuker, B. S. Chang, A. J. Minn, C. B. Thompson, and S. W. Fesik, "Structure of BCL-x_L-Bak peptide complex: recognition between regulators of apoptosis," *Science* **275**, 983–986 (1997).

10. T. Lindsten, A. J. Ross, A. King, W. X. Zong, J. C. Rathmell, H. A. Shiels, E. Ulrich, K. G. Waymire, P. Mahar, K. Frauwirth, Y. Chen, M. Wei, V. M. Eng, D. M. Adelman, M. C. Simon, A. Ma, J. A. Golden, G. Evan, S. J. Korsmeyer, G. R. MacGregor, and C. B. Thompson, "The combined functions of proapoptotic Bcl-2 family members Bak and Bax are essential for normal development of multiple tissues," *Mol. Cell* **6**, 1389–1399 (2000).
11. M. C. Wei, W. X. Zong, E. H. Y. Cheng, T. Lindsten, V. Panoutsakopoulou, A. J. Ross, K. A. Roth, G. R. MacGregor, C. B. Thompson, and S. J. Korsmeyer, "Proapoptotic BAX and BAK: a requisite gateway to mitochondrial dysfunction and death," *Science* **292**, 727–730 (2001).
12. E. H. Y. Cheng, M. C. Wei, S. Weiler, R. A. Flavell, T. W. Mak, T. Lindsten, and S. J. Korsmeyer, "BCL-2, BCL-XL sequester BH3 domain-only molecules preventing BAX- and BAK-mediated mitochondrial apoptosis," *Mol. Cell* **8**, 705–711 (2001).
13. A. Letai, M. C. Bassik, L. D. Walensky, M. D. Sorcinelli, S. Weiler, and S. J. Korsmeyer, "Distinct BH3 domains either sensitize or activate mitochondrial apoptosis, serving as prototype cancer therapeutics," *Cancer Cells* **2**, 183–192 (2002).
14. Z. N. Oltvai, C. L. Milliman, and S. J. Korsmeyer, "Bcl-2 heterodimerizes *in vivo* with a conserved homolog, Bax, that accelerates programmed cell death," *Cell* **74**, 609–619 (1993).
15. X. M. Yin, Z. N. Oltvai, and S. J. Korsmeyer, "BH1 and BH2 domains of Bcl-2 are required for inhibition of apoptosis and heterodimerization with Bax," *Nature (London)* **369**, 321–323 (1994).
16. A. Cuconati, C. Mukherjee, D. Perez, and E. White, "DNA damage response and MCL-1 destruction initiate apoptosis in adenovirus-infected cells," *Genes Dev.* **17**, 2922–2932 (2003).
17. S. N. Willis, L. Chen, G. Dewson, A. Wei, E. Naik, J. I. Fletcher, J. M. Adams, and D. C. S. Huang, "Proapoptotic Bak is sequestered by Mcl-1 and Bcl-xL, but not Bcl-2, until displaced by BH3-only proteins," *Genes Dev.* **19**, 1294–1305 (2005).
18. S. N. Willis, "Apoptosis initiated when BH3 ligands engage multiple Bcl-2 homologs, not Bax or Bak," *Science* **315**, 856–859 (2007).
19. J. Zheng, Y. Tsai, P. Kadimcherla, R. Zhang, J. Shi, G. A. Oyler, and N. N. Boustany, "The C-terminal transmembrane domain of Bcl-xL mediates changes in mitochondrial morphology," *Biophys. J.* **94**(1), 286–297 (2008).
20. K. Degenhardt, G. Chen, T. Lindsten, and E. White, "Bax and Bak mediate p53-independent suppression of tumorigenesis," *Cancer Cells* **2**, 193–203 (2002).
21. H. C. VandeHulst, *Light Scattering by Small Particles*, Dover, New York (1981).
22. H. J. Chae, J. S. Kang, J. O. Byun, K. S. Han, D. U. Kim, S. M. Oh, H. M. Kim, S. W. Chae, and H. R. Kim, "Molecular mechanism of staurosporine-induced apoptosis in osteoblasts," *Pharmacol. Res.* **42**(4), 373–381 (2000).
23. M. Giuliano, G. Bellavia, M. Lauricella, A. D'Anneo, B. Vassallo, R. Vento, and G. Tesoriere, "Staurosporine-induced apoptosis in Chang liver cells is associated with down-regulation of Bcl-2 and Bcl-X-L," *Int. J. Mol. Med.* **13**(4), 565–571 (2004).
24. A. Dunn and R. Richards-Kortum, "Three-dimensional computation of light scattering from cells," *IEEE J. Sel. Top. Quantum Electron.* **2**(4), 898–905 (1996).
25. J. Y. Zheng, R. M. Pasternack, and N. N. Boustany, "Optical scatter imaging with a digital micromirror device," *Opt. Express* **17**(22), 20401–20414 (2009).
26. J. R. Mourant, T. M. Johnson, S. Carpenter, A. Guerra, T. Aida, and J. P. Freyer, "Polarized angular dependent spectroscopy of epithelial cells and epithelial cell nuclei to determine the size scale of scattering structures," *J. Biomed. Opt.* **7**(3), 378–387 (2002).
27. J. D. Wilson and T. H. Foster, "Mie theory interpretations of light scattering from intact cells," *Opt. Lett.* **30**(18), 2442–2444 (2005).